sustainability

MDPI

Article

Study on Combustion Characteristics and Thermodynamic Parameters of Thermal Degradation of Guinea Grass (*Megathyrsus maximus*) in N_2-Pyrolytic and Oxidative Atmospheres

Ayokunle O. Balogun [1], Adekunle A. Adeleke [1,2,*], Peter P. Ikubanni [1,2], Samuel O. Adegoke [3], Abdulbaset M. Alayat [4] and Armando G. McDonald [4]

[1] Department of Mechanical Engineering, College of Engineering, Landmark University, Omu-Aran 251103, Nigeria; balogun.ayokunle@lmu.edu.ng (A.O.B.); ikubanni.peter@lmu.edu.ng (P.P.I.)
[2] SDG-9 (Industry, Innovation, and Infrastructure) Research Group, Landmark University, Omu-Aran 251103, Nigeria
[3] Department of Petroleum Engineering, Faculty of Engineering and Technology, University of Ibadan, Ibadan 200284, Nigeria; sfikayo@gmail.com
[4] Department of Forest, Rangeland and Fire Science, University of Idaho, Moscow, ID 83844-1132, USA; alay0843@vandals.uidaho.edu (A.M.A.); armandm@uidaho.edu (A.G.M.)
* Correspondence: adeleke.kunle@ymail.com

check for updates

Citation: Balogun, A.O.; Adeleke, A.A.; Ikubanni, P.P.; Adegoke, S.O.; Alayat, A.M.; McDonald, A.G. Study on Combustion Characteristics and Thermodynamic Parameters of Thermal Degradation of Guinea Grass (*Megathyrsus maximus*) in N_2-Pyrolytic and Oxidative Atmospheres. *Sustainability* **2022**, *14*, 112. https://doi.org/10.3390/su14010112

Academic Editors: Farhad Taghizadeh-Hesary and Han Phoumin

Received: 2 November 2021
Accepted: 1 December 2021
Published: 23 December 2021

Publisher's Note: MDPI stays neutral with regard to jurisdictional claims in published maps and institutional affiliations.

Copyright: © 2021 by the authors. Licensee MDPI, Basel, Switzerland. This article is an open access article distributed under the terms and conditions of the Creative Commons Attribution (CC BY) license (https://creativecommons.org/licenses/by/4.0/).

Abstract: This study provides an extensive investigation on the kinetics, combustion characteristics, and thermodynamic parameters of the thermal degradation of guinea grass (*Megathyrsus maximus*) in N_2-pyrolytic and oxidative atmospheres. A model-fitting technique and three different iso-conversional techniques were used to investigate the kinetics of the thermal process, after which an analysis of the combustion characteristics and thermodynamic parameters was undertaken. Prior to this, experiments on the physico-chemical characterization, thermogravimetric, and spectroscopic analyses were carried out to provide insight into the compositional structure of the guinea grass. The volatile matter, fixed carbon, and total lignin contents by mass were 73.0%, 16.1%, and 21.5%, respectively, while the higher heating value was 15.46 MJ/kg. The cellulose crystallinity index, determined by XRD, was 0.43. The conversion of the GG in air proceeded at a relatively much higher rate as the maximum mass-loss rate peak in a 20 K/min read was −23.1 and −12.3%/min for the oxidative and the pyrolytic, respectively. The kinetics investigation revealed three distinctive stages of decomposition with their corresponding values of activation energy. The average values of activation energy (FWO) at the latter stages of decomposition in the pyrolytic processes (165 kJ/mol) were higher than those in the oxidative processes (125 kJ/mol)—an indication of the distinctive phenomenon at this stage of the reaction. The Coats–Redfern kinetic model revealed that chemical reactions and diffusional models played a predominant role in the thermal decomposition process of the GG. This study showed that the thermodynamic parameters varied with the conversion ratio, and the combustion performance increased with the heating rates. The use of GG as an energy feedstock is recommended based on the findings from this work.

Keywords: physico-chemical characterization; Coats–Redfern model; flammability; integral model; iso-conversional

1. Introduction

The excessive utilization of fossil fuel sources for diverse energy purposes engenders a grave global concern. The combustion of these fuel sources results in the emission of greenhouse gases (GHGs), which have been implicated in global warming and climate change phenomena [1,2]. Again, fossil fuels, which are non-renewables, are being heavily depleted due to an increasing rate of exploitation. Consequently, attention is shifting more

toward biomass resources because they are viewed as carbon neutral and abundantly available as inexpensive residues, and they possess widespread availability and huge sustainability potential. It has been reported that energy from biomass has replaced about 14% of the global energy consumption [1]. Diverse biomass materials have been investigated through thermochemical means for probable bioenergy applications and biofuel production. These include rice husk, corn cobs [3], sugarcane straw [4], peanut shells [1], sorghum bicolor glume [5], coffee residues [6], and different woody samples [7–9]. Recently, interest has been turning toward the exploration of different energy crops, which include diverse varieties of grass species, for thermal analysis [10–12].

There are a number of reasons for the recent keen interest in the use of grasses as feedstock materials for biofuel production. The interest may have been prompted by the availability of large expanses of degraded lands, upon which grasses can be cultivated in some reclamation efforts. For instance, Cai et al. [13] stated that about 1107–1411 Mha of degraded land is available globally for the cultivation of energy crops. Grasses have also been identified as short-rotation, non-food crops, as well as low-input, high-yielding biomasses [11,14]. For example, relative to corn feedstock, which has a yield of about 7 Mg/(ha*year), the yield of grasses could reach as high as 40 Mg/(ha*year) [15,16]. This makes them viable substitutes for alleviating the unwholesome competition that arises from the use of food crops, such as corn and sugarcane, for biofuel production. It was noted that, in 2014, 91 billion liters of bioethanol was produced worldwide, mainly through the physicochemical processing of grains and sugarcane—stirring ethical issues from the public [11]. Another attraction to grasses is that though woody biomass residues have been widely investigated, relative to grass their use is characterized by some challenges that include limited land availability, a low annual biomass yield, a slow growth rate, and difficulty in harvesting due to higher energy requirements [14]. Guinea grass (*Megathyrsus maximus*), in particular, has a reputation for being a prolific energy crop in the sub-Saharan region of Africa. It exhibits rapid growth, tolerance to low soil fertility, and resistance to adverse weather conditions [17]. Aside from these characteristics, it is also a lignocellulosic biomass whose polymeric structure is characterized by an intricate matrix of hemicellulose, cellulose, and lignin constituents.

It is important to note that the polymeric structure of grasses differs significantly as a function of certain factors, such as grass variety, maturity stage, and environmental conditions [15]. In terms of climatic conditions, grasses may be broadly classified as tropical (C4) or temperate (C3) region grasses. The major constituents of the former are sucrose and starch, while the latter is predominantly rich in fructose and sucrose [15]. Specifically, it has been noted that *Miscanthus* x *giganteus*, a native Asian grass, has the distinctive feature of a high lignocellulose yield—hemicellulose (20–40%), cellulose (40–60%), and lignin (10–30%) [18]. In contrast, the polymeric constituents of Napier grass (native to Africa) and Bermuda grass (mainly grown in the United States) are comparable to the one mentioned earlier. Switch grass exhibits a slightly different structural composition—the hemicellulose, cellulose, and lignin, respectively, are 25–29%, 37–40%, and 18–25% [15]. Relative to the previous grasses, tall fescue, timothy, yellow flag, and meadow foxtail show markedly different compositions (Table 1). From the foregoing discussion, grasses represent a suitable lignocellulosic feedstock for biofuel production. However, given the wide variation in their structural makeup, it is imperative to undertake detailed characterization analyses prior to deployment for bioenergy purposes. Not only does the information from such analyses provide valuable insight into the chemical character of the feedstock, but it is also profoundly useful in the design of reactors and the modeling and optimization of the associated thermal processes.

Table 1. Polymeric composition of selected grasses [15].

Grasses	Polymeric Composition			Place of Origin
	Cellulose (%)	Hemicellulose (%)	Lignin (%)	
Tall fesecue	25	25	14	Large parts of Europe, Asia, and North Africa
Timothy	28	30	11.5	US, Canada, Europe
Yellow flag	28	10	7	Europe, Western Asia, Northwest Africa
Meadow foxtail	28–31	15–18	11–15	England and Wales

The basic characterization efforts, including proximate and ultimate analyses and higher heating value (HHV) determination, have been utilized extensively in evaluating the composition of diverse biomass feedstock [6,19,20]. The wet chemistry method, typically based on a two-step acidic hydrolysis, is an analysis that has proven reliable in providing insight into biomass composition. However, it is time-consuming and labor-intensive and requires pre-conditioning [21]. Another notable method is infra-red spectroscopic analysis. It is a powerful technique that can be utilized for gathering both quantitative and qualitative data. It is a non-destructive test that is fast and precise. In addition, it is devoid of elaborate sample preparation and the use of expensive and dangerous chemicals. Balogun et al. [22] subjected brewer's spent grain (BSG) to pyrolysis and then undertook the physico-chemical, thermal, and spectroscopic analyses of the BSG and its biochar. They reported a significant variation between the structural configuration of the original BSG and its biochar based on the condensation index and the cellulose crystallinity content. Research has been conducted on the comprehensive characterization of five different biomass samples and revealed that there were distinct differences in the chemical and structural constituents of the samples [23].

Notably, the thermogravimetric analysis (TGA) represents another critical characterization technique that provides a rich source of information regarding the thermal behavior of lignocellulosic biomass. The thermal decomposition of a solid by TGA can be performed isothermally, or otherwise, in an inert or oxidative atmosphere. From the TGA data, deductions can be made on the decomposition mechanism, the kinetic and thermodynamic parameters, and the combustion characteristics of a sample. Though kinetic investigation is suitable for small-sized particles and low-heating-rate processes, it has been widely used because of its high predictability and simplicity. Furthermore, the kinetic data produce sub-models that can be incorporated into complex transport phenomena models to yield practical descriptions of either pyrolysis or combustion processes. The kinetic models, including the one-step global kinetic model, the independent parallel and competitive reaction models, the detailed lumped kinetic model, and the distributed activation energy model, have been formulated and extensively applied [24,25]. Typically, in a kinetic study, the reaction rate is given as a function of temperature and the conversion ratio, and the temperature dependence is expressed as an Arrhenius' equation. The best-fit model, applied to the TGA data, is utilized for the determination of the kinetic parameters and subsequently for simulation. The mathematical approach deployed for solving the rate equation results in two notable techniques, namely iso-conversional and model fitting.

In the model-fitting technique, prior knowledge of the reaction mechanism is required for the selection of an appropriate reaction model. This is achieved by successively fitting different reaction models to the TGA data to select the one with the highest correlation. A popularly utilized model-fitting method is the Coats–Redfern (CR) integral technique. The kinetics of solid-fuel pyrolysis was analyzed using the CR technique and the model identified the probable reaction mechanisms at different stages of pyrolysis [26]. The direct differential and CR methods were deployed to deduce the non-isothermal kinetic parameters of the pyrolysis of pure and crude glycerol, and the distinctive activation energy values were observed [27]. There have been more recent comparative kinetics studies that involved the CR model-fitting method [8,28–31]. The iso-conversional technique, on the

other hand, forestalls the need for any foreknowledge of the reaction mechanism. Rather, it relies on the use of several TGA measurements at varied heating rates for the evaluation of the kinetic parameters, and it is based on an approximation technique of the temperature integral. Some kinetic modeling studies have been undertaken through iso-conversional methods, including the Kissinger, Starink, Kissinger–Akahira–Sunose (KAS), and Flynn–Wall–Ozawa (FWO) models [7,25]. It has been demonstrated that thermal degradation of biomass follows a multi-step reaction mechanism because the kinetic parameters vary with the conversion degree [22,30,32].

Globally, energy recovery from biomass is predominantly from combustion processes (about 90%) [33]. Biomass combustion can yield low GHG emissions with efficient monitoring and control. Therefore, the combustion characteristics of specific biomass feedstock need to be quantified for the optimum design and modeling of the combustors and scrubbers. Furthermore, it is also critical to gather information on the feasibility of thermal-conversion processes as well as the energy measurements. This can be achieved by calculating the changes in enthalpy, Gibbs free energy, and entropy from the kinetic parameters [34]. There is limited information on the thermal decomposition of grasses of tropical origin. The objective of this study was to thermally decompose guinea grass in inert and oxidative environments, with the focus on evaluating the kinetic and thermodynamic parameters and the combustion characteristics. The kinetic study will entail the use of model-fitting and iso-conversional techniques, while the feedstock characterization will involve proximate, elemental, compositional, and spectroscopic analyses.

2. Materials and Methods

2.1. Materials

The guinea grass (GG) samples were harvested in an outdoor field (8°7′14″ N; 5°4′56″ E) within the Landmark University premises in June 2020. The grasses (of about 1–1.5 m tall) were initially air dried for 2 weeks and then oven dried at 70 °C for 24 h for ease of pulverization. The sample was pulverized in a ball mill and sieved into 0.6 and 1.18 mm particle sizes with the aid of a mechanical sieve. The 0.6 mm screened particles were used for chemical and TGA characterization. The cellulose (Whatman CF1, Maidstone, England), xylan from corn (TCI America, Portland, OR, USA), softwood kraft lignin (Indulin AT, Meadwestvaco, Charleston, SC, USA), and hardwood organosolv lignin (Lignovate LLC, Fayetteville, AR, USA) were used as received.

2.2. Biomass Characterization

The HHV was determined using a Parr oxygen bomb calorimeter (model 1261, Modline, IL, USA) on densified GG samples (1.0 g, 6 mm diameter using a Carver laboratory press (Wabash, IN, USA) at 68 MPa) according to ASTM D5865-04. The ash content, volatile matter (VM), and fixed carbon (FC) for GG were evaluated based on proximate analysis (ASTM E870-82). The elemental analysis was conducted on a Costech ESC 4010 elemental analyzer (Valencia, CA, USA) to obtain the C and N contents.

The GG sample (4.0 g) was submitted to Soxhlet extraction using CH_2Cl_2 (150 mL) for 16 h, and the extractives content was determined gravimetrically, according to ASTM D1108-96. The CH_2Cl_2 extract was analyzed for lipid profiles as their fatty acid methyl ester (FAME) derivatives after acidic methanolysis (2 mL of $CH_3OH/H_2SO_4/CHCl_3$ (1.7:0.3:2.0 $v/v/v$) at 90 °C for 90 min) and subsequent gas chromatography-mass spectrometry analysis (Thermoscientific ISQ-Trace1300 (Madison, WI, USA); Phenomenex (Torrance, CA, USA) ZB5 30 m x 0.25 mm column; 40 °C (1 min) to 280 °C at 5 °C/min) [22]. The extractive-free GG (200 mg) was subsequently analyzed for lignin and carbohydrate contents by acid hydrolysis [72% H_2SO_4 (2 mL), 60 min, 30 °C], followed by secondary hydrolysis [4% H_2SO_4, 30 min, 121 °C] in an autoclave, according to ASTM D 1106-96. The Klason lignin content was evaluated gravimetrically after filtration. Acid soluble lignin was determined at 205 nm of the filtered hydrolysate (250 mL), using an extinction coefficient of 110 L g^{-1} cm^{-1} (Genesys 50, ThermoScientific, Hanover Park, IL, USA). The hydrolysis

filtrate (5 mL) was subjected to carbohydrate analysis according to ASTM E 1758-01. The monosaccharides were quantified by HPLC (two Rezex RPM columns, 7.8 mm × 300 mm, Phenomenex, Torrance, CA, USA) at 85°C on elution with water (0.5 mL min^{-1}) using differential refractive index detection (Waters model 2414, Milford, MA, USA). All analyses were performed in duplicate.

FTIR spectroscopy was conducted on an iS5 spectrometer (ThermoNicolet, Madison, WI, USA) in the single bounce attenuated total reflection (ATR) mode (iD5, ZnSe). The determination of the lignin syringyl/guaiacyl (S/G) ratio was conducted at the relative band intensities at 1462 and 1508 cm^{-1}. The relative band intensities at 1370 and 2900 cm^{-1} were used in determining cellulose crystallinity as the total crystalline index (TCI). [7]. The cellulose lateral order index (LOI) was determined from band intensity ratios at 1430 and 897 cm^{-1} [35]. XRD was carried out on a Siemens D5000 diffractometer (Karlsruhe, Germany) (2θ from 5 to 50° with steps of 0.2°). The diffractogram was peak fitted using Origin software prior to determination of the cellulose crystallinity index (CCI = $(1 - (I_{am}/I_{002}))$, where I_{am} is the intensity of the peak at 2θ = 15° and I_{002} is the maximum intensity of the (002) plane diffraction at 2θ = 22°) [22].

2.3. Thermogravimetric Analysis (TGA)

The GG sample with an initial mass of 5.44 ± 0.25 mg was subjected to dynamic heating experiments in a Perkin Elmer TGA-7 (Waltham, MA, USA) instrument in either an N_2 or dry air environment at a flow rate of 30 mL/min. The heating temperature was raised from ambient conditions (29.15 ± 0.64 °C) to 900 °C at three heating rates (5, 10, and 20 °C/min), and the data obtained were analyzed using the Pyris v11 software. The experiments were performed in duplicate.

2.4. Kinetic Modelling

The rate equation for a single-step global kinetic model for solid-state degradation under isothermal heating is given as Equation (1).

$$\frac{d\theta}{dt} = Aexp^{(-\frac{E}{RT})}\, f(\theta) \tag{1}$$

where R is the universal gas constant (8.314 J/(mol*K), $f(\theta)$ is the differential decomposition model, A = pre-exponential frequency factor, and θ is the conversion degree expressed as Equation (2).

$$\theta = \frac{W - W_i}{W_f - W_i} \tag{2}$$

The W, W_i, W_f, respectively, are sample mass (%) at temperature T, initial mass, and residual mass. Inserting the constant linear heating rate, $\beta = \frac{dT}{dt}$, into Equation (1) yields the dynamic heating condition (Equation (3)):

$$\frac{d\theta}{dT} = \frac{A}{\beta}exp^{(-\frac{E}{RT})}\, f(\theta) \tag{3}$$

2.4.1. Coats–Redfern (CR) Method

The ordinary differential equation in Equation (3) can be handled by integration by separation of the variable to obtain a temperature integral function as shown in Equation (4). However, an analytical solution is not attainable.

$$g(\theta) = \int_0^\theta \frac{d\theta}{f(\theta)} = \int_{T_0}^T \frac{A}{\beta}exp^{(-\frac{E}{RT})}\, dT \tag{4}$$

Note that $g(\theta)$ represents an integral decomposition model that represents the reaction mechanism that relates to the solid-state degradation. A couple of such models are given

in Table 2. The logarithmic transformation of Equation (3) alongside Equation (4) yields the CR model for the derivation of the kinetic parameters, as shown in Equation (5):

$$\ln\left(\frac{g(\theta)}{T^2}\right) = \ln\frac{AR}{\beta E}\left(1-2\frac{RT}{E}\right) - \frac{E}{RT} \tag{5}$$

Table 2. Empirical correlations for $g(\theta)$ on different reaction mechanisms [28,29].

Mechanism Model	$g(\theta)$
Power Law (n = 1, 2, 3)	$\theta^{1/n}$
Nucleation Reaction Models	
Avarami-Eroféve (n = 1.5, 2, 3)	$[-\ln(1-\theta)]^{1/n}$
Contracting sphere	$1-(1-\theta)^{1/2}$
Contracting cylinder	$1-(1-\theta)^{1/3}$
Diffusional Models	
1-D diffusion	θ^2
2-D diffusion	$[(1-\theta)\times\ln(1-\theta)]+\theta$
3-D diffusion-Jander	$\left[1-(1-\theta)^{1/3}\right]^2$
3-D diffusion-GB	$1-\frac{2\theta}{3}-(1-\theta)^{2/3}$
Chemical Reaction Models	
1st order	$-\ln(1-\theta)$
n-th order	$\left[1-(1-\theta)^{1-n}\right]/(1-n)$

The plot of the left-hand side of Equation (5) against the reciprocal of temperature yields, approximately, a linear curve from whose slope the activation energy can be obtained. It is assumed that $RT \ll E$; therefore, the intercept is given as $intercept = \ln\frac{AR}{\beta E}$, from which the pre-frequency factor is computed.

2.4.2. Differential Friedman Method (DFM)

If the natural logarithm is applied to Equation (3), it yields Equation (6), which is commonly referred to as the differential Friedman's kinetic model.

$$\ln\left[\frac{d\theta}{dt}\right] = \ln\left[\beta\left(\frac{d\theta}{dT}\right)\right] = \ln[Af(\theta)] - \frac{E}{RT} \tag{6}$$

In Friedman's relation, the conversion function, $f(\theta)$, is assumed constant. This implies that the solid-state degradation is primarily dependent on the mass-loss rate and is independent of the temperature. The linear plot of $\ln\left[\frac{d\theta}{dt}\right]$ against $\frac{1}{T}$ is generated for different heating rates, and the activation energy is determined from the slope $\left(slope = -\frac{E}{R}\right)$. It is important to note that the use of the derivative conversion data makes the DFM prone to noise sensitivity and numerical instability, and therefore, caution must be exercised in the data interpretation [36].

2.4.3. Flynn–Wall–Ozawa (FWO) Method

The FWO model takes the apparent activation energy to be constant during the thermal decomposition process and engages Doyle's relation to approximate the temperature integral function. Taking the logarithm of the integral function and inserting Doyle's approximation yields Equation (7).

$$\log\beta = \log\left(A\frac{E}{Rg(\theta)}\right) - 2.315 - 0.4567\frac{E}{RT} \tag{7}$$

A plot of $\log\beta$ against $\frac{1}{T}$ for different heating rates produces straight lines. Again, the activation energy can be evaluated from the slope of the lines as $\left(slope = -0.4567\frac{E}{R}\right)$.

2.4.4. Starink (STK) Method

The Starink method is based on the optimization of two iso-conversional methods, namely the Flynn–Wall–Ozawa and the Kissinger–Akhira–Sunose (KAS), and it is expressed as Equation (8).

$$\ln\left(\frac{\beta}{T^{1.92}}\right) = C_s - 1.0008\frac{E}{RT} \tag{8}$$

A plot of $\ln\left(\frac{\beta}{T^{1.92}}\right)$ against the reciprocal of temperature generates linear curves and the activation energy can be computed from their slopes. It was noted that Starink's model presented an accuracy of an order of magnitude higher than the FWO and KAS.

2.4.5. Combustion Characteristics Indices

The indices, ignition temperature (T_i), the temperature at the maximum DTG (T_{max}), the burnout temperature (T_b), the corresponding time (t_i, t_{max}, t_b), and the maximum and average DTG ($-R_p$ and $-R_v$), can be obtained from the TGA data [1,8]. These were subsequently used to monitor the combustion characteristics, comprehensive combustibility (S), flammability (C), ignition (D_i), and burnout (D_b), according to the relations in Equations (9)–(12).

$$S = \frac{-R_p \times -R_v}{T_i^2 \times T_b} \tag{9}$$

$$C = \frac{-R_p}{T_i^2} \tag{10}$$

$$D_i = \frac{-R_p}{t_i \times t_b} \tag{11}$$

$$D_b = \frac{-R_p}{\Delta t_{1/2} \times t_p \times t_b} \tag{12}$$

2.4.6. Thermodynamic Analysis

The thermodynamic parameters [change in enthalpy (ΔH, J/mol), Gibbs free energy (ΔG, J/mol), and entropy (ΔS,J/((mol*K)))] were deduced as functions of conversions from the kinetic parameters, as shown in Equations (13)–(15).

$$\Delta H = E_\theta - RT \tag{13}$$

$$\Delta G = E_\theta + RT_{max}\ln\left(\frac{k_B T_{max}}{hA_\theta}\right) \tag{14}$$

$$\Delta S = \frac{\Delta H - \Delta G}{T_{max}} \tag{15}$$

where k_B, and h are the Boltzmann constant (1.381×10^{-23} J/K) and the Planck constant (6.626×10^{-34} J s), respectively.

3. Results and Discussion

3.1. Characterization of Guinea Grass

Table 3 shows the results of the proximate, elemental, compositional, and calorific value analyses of the GG. It is shown that the GG contained 40% C, 1.3% N, and 5.1% ash. The ash content was well within the range reported for other grass species, such as Elephant grass [37], Camel grass (6.31%) [38], and *Echinochloa stagnina* (6.31%) [23], as well as other biomass wastes, such as jackfruit peel (5.56%) and seeds (6.64%) [39]. In comparison to low-rank coals, the lower ash content of biomass makes it more suitable for combustion processes [39]. This is due to technical problems, such as slagging and fouling, which impede heat and mass transfer. The estimated protein content of 8.1% was in the range (5.3–8.8%) for fresh GG, as documented by Aganga and Tshwenyane [40]. An FC value

of 16.1% was in the range (8.5–16.9%) for Napier grass [41]. The calorific value obtained for the GG was 15.5 MJ kg^{-1}, and is comparable to Napier grass (16.2–18.1 MJ kg^{-1}) [41], tamarind residues (17.5 MJ kg^{-1}) [42], smoked cigarette butts (18.5 MJ kg^{-1}) [43], and jackfruit wastes (16.3–17.2 MJ kg^{-1}) [39]. An extractives content of 1.4% agreed with the literature [40,44]. A lignin content of 21.5%, which was nearly twice that reported by Ratsamee et al. [45] for GG, using the acetyl bromide method, was recorded, while Mohammed et al. [41] obtained a lignin content for Napier grass of 24%. The higher lignin value is attributable to protein interference in the Klason lignin determination of grasses [46]. Detailed carbohydrate analysis showed mainly glucan (34%) and xylan (18%), together with galactan (1.2%) and arabinan (6.4%). The total carbohydrate value is lower than that reported by Ratsamee et al. (hemicellulose (27.1%) + cellulose (41.7%)) for GG [45], but higher than for the other grasses listed in Table 1 [15]. The variations observed in some parameters may be due to differences in genetics and/or environmental conditions.

Table 3. Proximate, Elemental, and Compositional data for GG sample.

Parameter	GG
Proximate Analysis	
Volatile matter (VM) (%)	73.0 ± 0.3
Fixed carbon (FC) (%)	16.1 ± 0.8
Ash (%)	5.09 ± 0.01
Elemental Analysis	
C (%)	40.1 ± 0.4
N (%)	1.30 ± 0.01
Protein (N * 6.25) (%)	8.12 ± 0.08
Compositional Analysis	
CH_2Cl_2 extractives (%)	1.41 ± 0.03
Acid soluble lignin (%)	3.4 ± 0.2
Klason lignin (%)	18.1 ± 0.5
Total lignin (%)	21.5 ± 1.5
Glucan (%)	33.6 ± 0.5
Xylan (%)	17.7 ± 0.5
Galactan (%)	1.2 ± 0.4
Arabinan (%)	6.4 ± 0.4
Total Neutral sugar (%)	58.9
HHV (MJ kg^{-1})	15.46 ± 0.16

Fatty acids are an important source of unsaturated acids in grasses for foraging animals [47]. The fatty acid profile of GG extractives was determined as FAME derivatives and given in Table 4. The fatty acids were from C_{12} (lauric acid) to C_{24} (lignoceric acid), with the most abundant being palmitic acid (74 mg/g extract), linoleic (39 mg/g extract), and oleic (24 mg/g extract) acids. Lauric (C12) to stearic (C18) acids, saturated and unsaturated, have been observed in several types of forage grass [47].

Table 4. Fatty acid profile of GG extract.

FAME	RT (min)	M^+ (m/z)	Concentration (mg/g Extract)
Lauric acid (C12:0)	24.15	214	8.13
Myristic (C14:0)	28.69	242	7.16
Pentadecanoic acid (C15:0)	30.79	256	2.22
Palmitelaidic acid (16:1)	32.31	268	3.26
Palmitic acid (C16:0)	32.83	270	74.4
Heptadecanoic acid (C17:0)	34.83	284	3.51
Linoleic acid (C18:2)	35.84	294	39.4

Table 4. *Cont.*

FAME	RT (min)	M^+ (m/z)	Concentration (mg/g Extract)
Oleic acid (C18:1)	36.00	296	23.9
Stearic acid (C18:0)	36.54	298	6.93
Arachidic acid (C20:0)	40.00	326	3.18
Behenic acid (C22:0)	43.14	354	4.10
Tricosanoic acid (C23:0)	44.82	368	2.08
Lignoceric acid (C24:0)	46.85	382	4.69

Cellulose crystallinity is a key factor in the biological or thermal degradability of biomass. The XRD analysis of the GG (Figure 1a) showed a typical diffractogram of cellulose I, with 2θ peaks at 15° and 22°, which were assigned to the cellulose planes of (101) and (002), respectively [22]. The CCI was determined after peak fitting at 0.431, and it was found to be higher than that of Napier grass, having a CCI of 0.327 [46].

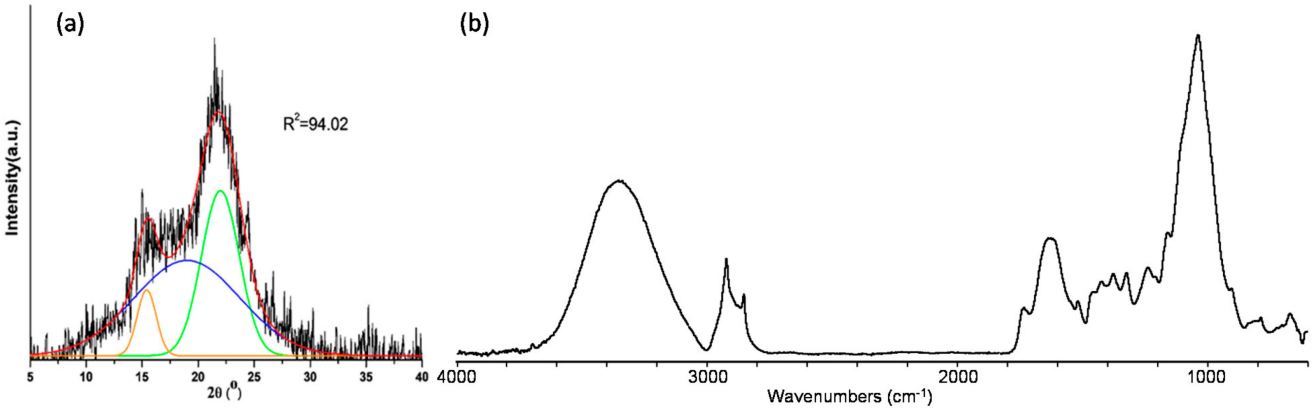

Figure 1. (**a**) X-ray diffractogram and (**b**) FTIR spectrum of guinea grass.

The GG was analyzed for chemical properties by FTIR spectroscopy (Figure 1b). The vibrational band assignments in GG by Balogun et al. [22] were used. An O-H stretching band around 3300 cm^{-1} was assigned to the polysaccharides and lignin. The C–H stretching band at 2920 cm^{-1} was assigned to the aliphatic structures, while the carbonyl band around 1735 cm^{-1} was assigned to the acetyl and uronic acid groups in xylan. The presence of lignin was confirmed by the distinct bands at 1514 and 1604 cm^{-1}, assigned to the aromatic skeletal vibrations. The large band centered at 1037 cm^{-1} was assigned to the C-O stretching in the cellulose, hemicellulose, and lignin polymers. As mentioned earlier, cellulose degradation is associated with its crystallinity. Cellulose crystalline information was determined by its TCI (crystallinity) and LOI (cellulose I), and the values obtained were both 1.1 for the GG. The values of TCI and LOI for Napier grass were 1.25 and 0.53, respectively [48], while sorghum glume has a lower value of LOI (0.75) [49]. The glass transition temperature (softening point) and reactivity of lignin are influenced by its S/G ratio [34]. The lignin S/G ratio of GG was calculated at 1.2, and it was higher than straw soda lignin (1.05) [49]. Sun et al. [34] used Raman spectroscopy to determine S/G ratios for switchgrass (0.92) and maize (1.1).

3.2. Thermal Degradation Characteristics of GG at Different Heating Rates

Figure 2a,b present the thermograms of GG in the N_2 and air atmospheres, respectively, at different heating rates.

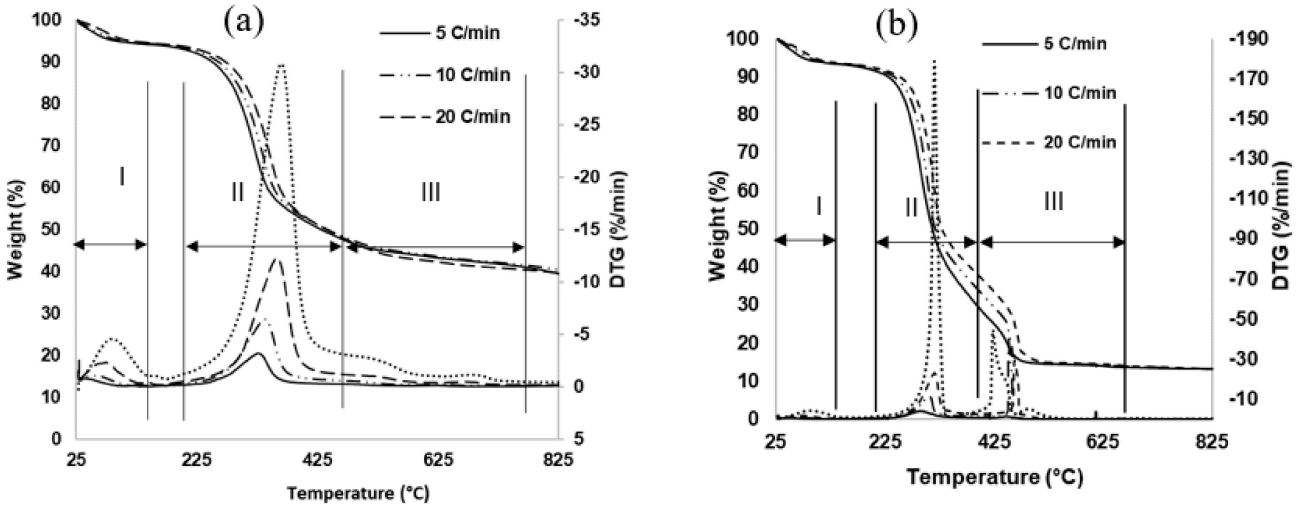

Figure 2. Thermograms of mass loss and mass-loss rate (DTG) for GG in (**a**) N_2 and (**b**) air atmospheres.

The thermograms for the thermal degradation of GG in N_2 and air reveal that the degradation trend consists mainly of three regions, namely dehydration (I), devolatilization (II), and solid burnout or char formation (III). The first region is often ascribed to moisture loss and occurs below 100 °C for all heating rates. Shortly after, around 220 °C, is a characteristic "shoulder" that is indicative of hemicellulose degradation. Of the polymeric constituents, it is the least stable and thus the most reactive. Prior to the "shoulder", between 140 and 200 °C, a mass loss of less than 1% is noted. This may be due to the breakdown of some low-molecular organics with very weak bonds. At around 290 and 370 °C, a sharp and conspicuous DTG peak emerges. This is typically assigned to cellulose degradation because, as it has been noted, at temperatures above 250 °C cellulose is totally decomposed [22]. The devolatilization region is where substantial parts of the bonds in hemicellulose and cellulose and partly in lignin are deconstructed, leading to a release of large amounts of volatiles. This notion is supported by other researchers who have also observed that this region is suggestive of a simultaneous decomposition of the hemicellulose, cellulose, and lignin components [8]. Lignin decomposes over a wide range of temperatures, and thus, there is the trailing effect that extends to much higher temperatures. At about 600 °C, a barely visible peak appears—this may be indicative of the deconstruction of lignin's strongest bonds and/or the thermal cracking of some of the condensed lignin structures formed from the previous primary reactions [50].

Figure 3 depicts the thermograms of the isolated polymeric constituents (xylan, cellulose, and lignin (softwood and hardwood)), and the GG decomposition under N_2 conditions at 20 °C/min. This provides insight into the sequence of the decomposition of the lignocellulosic biomass constituents. It is shown that hemicellulose (xylan) is the most reactive with a DTG peak at about 270 °C. Then, cellulose appears, with a prominent DTG peak at about 400 °C, which is closely followed by lignin. There are quantitative variations in terms of the DTG peaks (height and temp) between the different constituents, and these affirm the discussion on the trend observed for GG thermal decomposition. The apparent discrepancy may be due to the fact that the isolated constituents are devoid of the complexity associated with the lignocellulosic macromolecular structure in their natural matrix.

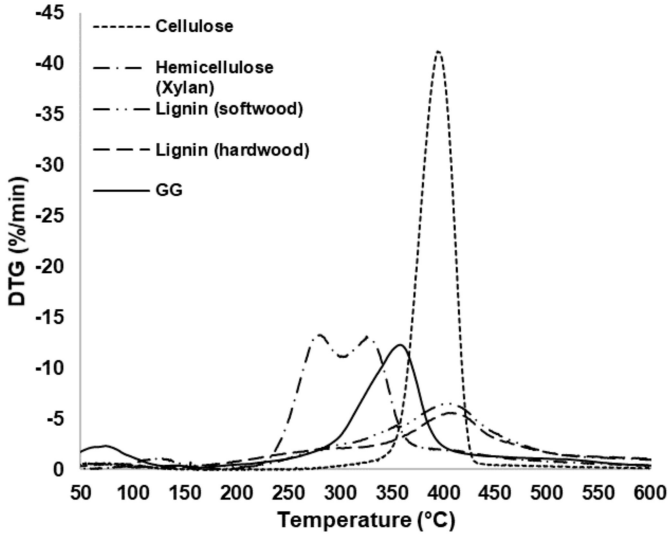

Figure 3. Thermograms of mass-loss rate (DTG) of cellulose, xylan, lignin, and GG in N_2 atmosphere at 20 °C/min.

Table 5 presents the thermal characteristics data from the decomposition of the GG in both atmospheres. A marginal difference exists in the residual mass as the heating rate rises for the decomposition in both the N_2 and the air atmosphere—this underscores the independence of the mass-loss trend on the heating rate. Similar trends have been shown in previous findings for peanut shells [1] and other biomass residues [3] in N_2 and air atmospheres. It is also demonstrated that the DTG peaks increase in height and shift to higher temperatures with an increase in the heating rate. For instance, the maximum DTG peaks in absolute terms for N_2 at 5, 10, and 20 °C/min read 3.21%/min (327 °C), 6.45%/min (339 °C), and 12.3%/min (358 °C), respectively. This is consistent with findings from the published literature for the pyrolysis and combustion of tobacco wastes [51]. This could be due to the heat transfer limitations that arise from the successive rise in the thermal gradient. This phenomenon usually occurs when there is rapid heating at the exterior relative to the inner parts of the sample, thus pushing the decomposition temperature to higher values [3].

Table 5. Heating rate, maximum peak temperature, residual mass, and mass-loss rate of GG decomposition under N_2 and air atmosphere.

	N_2			Air		
β	T_{max} (°C)	DTG (%/min)	R_w (%)	T_{max} (°C)	DTG (%/min)	R_w (%)
5	40.2	−0.80	28.7	48.5	−0.64	13.2
	326.9	−3.21		289.7	−4.15	
				447.4	−1.42	
	617.7	−0.15		638.0	−0.14	
10	58.0	−1.09	28.8	64.0	−1.08	13.2
	338.5	−6.45		307.3	−11.2	
				451.9	−40.6	
	642.3	−0.26		649.3	−0.20	
20	74.2	−2.33	29.8	74.8	−1.96	13.1
	358.3	−12.3		316.2	−23.1	
				462.9	−29.4	
Average			29.1 ± 0.6			13.2 ± 0.1

β = heating rate, T_{max} = maximum peak temperature, R_w = residual mass.

Specifically, the residual mass after thermal degradation in the air is far less than (above 100%) in N_2. This agrees with the findings from the published literature [3]. Thermal degradation in the air is an oxidative reaction (combustion), and it is expected to possess

a comparatively higher decomposition rate. This is further attested to by the mass-loss rate peak (DTG), which is shown to be much higher in the air atmosphere for the corresponding stages of degradation. For example, at this 20 °C/min the DTG peaks for the air and N_2 environments, respectively, read −23.1 and −12.3%/min. It is important to note that under air, a prominent peak appears at about 450 °C, as opposed to a very small peak under N_2. This conforms with the published data [8,52,53]. These observations suggest a thermal degradation phenomenon that is related to the combustion of char as char formation is predominant in the latter stage of oxidative degradation processes [8,52].

3.3. Kinetic Modeling

3.3.1. Model-Free Technique

Figure 4a,b, respectively, show the plots of the linear curves derived from the application of Equations (6)–(8) under N_2 and air conditions. The DFM, FWO, and STK models have proven suitable in predicting the kinetic parameters because of the high correlation ($R^2 > 0.9$) shown in both atmospheres. The plot was limited to a conversion degree, θ, ($0.15 \leq \theta \leq 0.8$) as this region is where the chemical reactions are predominant, and the kinetic models are more likely to produce realistic results. For the conversion range of 0.2 to 0.6, particularly for the integral methods (FWO and STK), the lines of best fit were approximately parallel. This may be an indication of a similar kinetic behavior in which the same reaction mechanism is exhibited for the specified range. In some cases, the non-parallel nature of the lines was largely restricted to either the earlier or the later part of the conversion. Perhaps, it is a pointer to a dissimilarity in the reaction mechanism that characterizes these decomposition stages. It has been suggested that the non-parallel nature of the linear fits could be an indication of a change in the reaction mechanism at a higher decomposition temperature [54,55]. Wang et al. [56] attributed it to the heterogeneity of the solid produced at the latter stages of degradation. The reaction mechanism at this stage is considered to involve a complex intertwine of diffusion, secondary reactions, and in situ catalysis of metals. It is also important to note that the non-parallel trend demonstrated by the DFM technique affirms the complexity of biomass decomposition, which arises from its intrinsically heterogenous character [55].

The dependence of activation energy, E_θ, on conversion ratio, θ, for the three isoconversional methods is displayed in Figure 5a,b for the N_2 and the air atmosphere, respectively. Table 6 also presents the E_θ, θ, and the coefficient of determination, R^2, data for both scenarios. These values were determined at an increment of 0.05 for θ, from 0.15 to 0.8. The E_θ had a significant positive correlation with θ ($r = 0.27$; $p < 0.05$). It has been noted that a significant variation in the apparent activation energy with conversion underscores the complexity associated with the kinetic process [57]. The effects of the decomposition atmospheres were also statistical analyzed, and it was shown that the E_θ was negatively correlated for air ($r = -0.25$; $p < 0.05$), while it was positively correlated for N_2 ($r = 0.84$; $p < 0.05$). The trend in the inert environment is different from that in the oxidative. In the inert scenario, the trajectories of the curves were similar, especially for the FWO and STK that are modeled according to the temperature integral approximation. The DFM is a differential technique that is not based on the integral approximation of the temperature function, and thus, it is relatively more accurate [36]. The E_θ versus θ plots show three distinct stages (Figure 5a). The first decomposition stage, θ = 0.15–0.2 for DFM, FWO, and STK presents average values of E_θ as 105, 101, and 98 kJ/mol, respectively. The degradation of the hemicellulose fractions is the predominant process at this stage due to its high reactivity relative to the other polymeric fractions. This may have accounted for the relatively low E_θ values [22]. Following a similar sequence, the average values of E_θ were evaluated as 137, 129, and 127 kJ/mol for θ = 0.25–0.6. At this stage, the combined contribution of the three polymeric constituents is more likely, albeit in different proportions. However, cellulose may be expected to play a significant role given its highly ordered crystalline nature that makes it stable thermally [22,51]. Again, this is corroborated by the earlier observation that cellulose degradation occurs within this period. In the

last reaction stage (θ = 0.65–0.8), the E_θ surges to much higher levels, recording average values of 189, 165, and 164 kJ/mol with the widest variability. Other researchers have reported similar trends for other lignocellulosic biomass [36,53]. The final decomposition stage for the pyrolytic processes is typically characterized by lignin and secondary product decomposition as well as char formation [22,51].

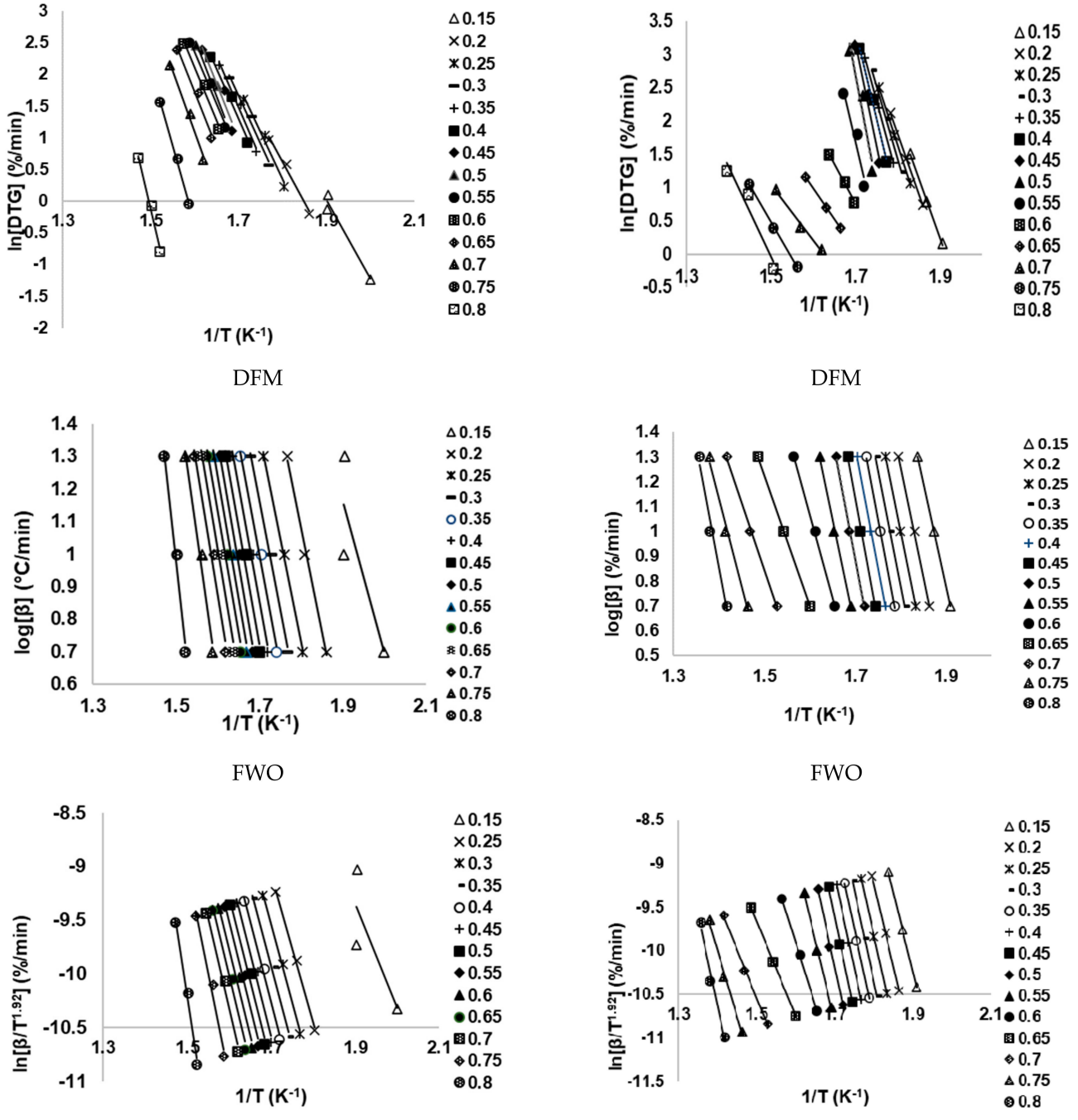

Figure 4. Plots of linear curves for DFM, FWO, STK models in (**a**) N_2 and (**b**) air environments.

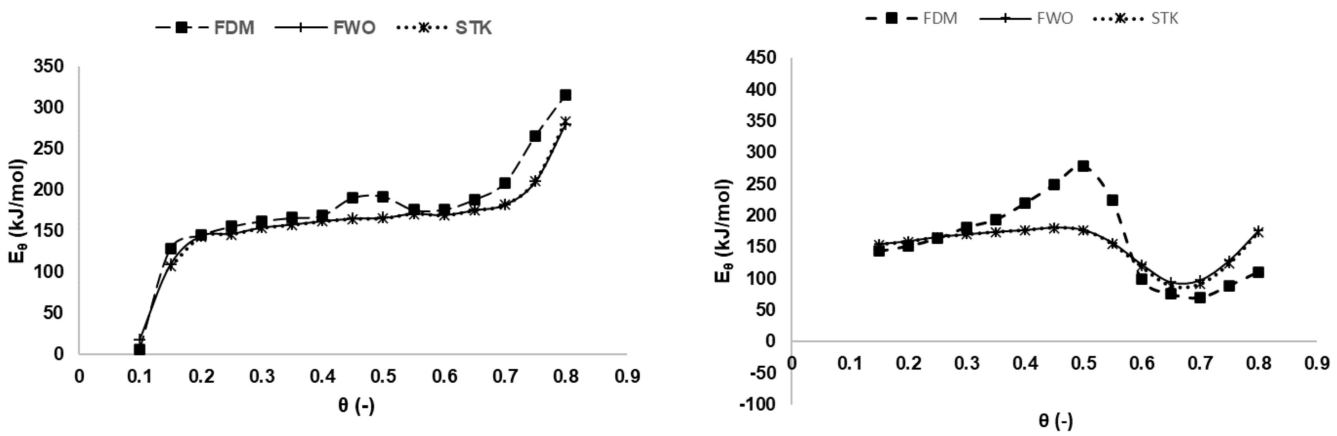

Figure 5. Plots of apparent activation energy, E_θ, against conversion ratio, θ, (**a**) N_2 and (**b**) air environments.

Table 6. Values of E_θ (kJ/mol), and R^2 for DFM, FWO, and STK models under N_2 and air environments.

	θ	N_2 DFM		N_2 FWO		N_2 STK		Air DFM		Air FWO		Air STK	
		E_θ (kJ/mol)	R^2	E_θ (kJ/mol)	R^2	E_θ (kJ/mol)	R^2	E_θ (kJ/mol)	R^2	E_θ (kJ/mol)	R^2	E_θ (kJ/mol)	R^2
STAGE I	0.15	105.3	0.969	84.7	0.916	80.9	0.694	143.8	0.997	155.2	0.999	154.7	0.999
	0.2	106.3	0.980	118.3	0.916	115.6	0.996	151.8	0.999	159.7	0.999	159.2	0.999
Average		105.8 ± 0.5		101.5 ± 16.8		98.2 ± 17.3		147.8 ± 5.2		157.5 ± 6.4		156.5 ± 6.5	
STAGE II	0.25	122.3	0.982	117.5	0.997	114.4	0.998	163.8	0.999	166.5	0.999	166.2	0.999
	0.3	128.2	0.983	123.3	0.992	120.3	0.994	181.6	0.999	170.6	0.999	170.4	0.999
	0.35	131.3	0.979	127.2	0.988	124.3	0.989	193.9	0.999	174.5	0.999	174.4	0.999
	0.4	132.8	0.977	130.9	0.986	128.1	0.987	219.5	0.993	177.2	0.998	177.2	0.997
	0.45	147.5	0.919	131.0	0.982	128.1	0.983	249.1	0.979	181.1	0.997	181.1	0.995
	0.5	152.1	0.913	132.9	0.982	130.0	0.983	279.1	0.935	177.4	0.997	177.1	0.996
	0.55	138.1	0.975	136.1	0.979	133.3	0.980	224.8	0.928	157.06	0.998	155.5	0.997
	0.6	139.9	0.973	135.8	0.976	132.9	0.977	100.2	0.992	122.9	0.998	119.3	0.999
Average		136.5 ± 9.3		129.3 ± 6.0		126.7 ± 6.1		201.5 ± 51.6		165.9 ± 17.7		162.0 ± 18.8	
STAGE III	0.65	147.2	0.976	138.9	0.974	136.1	0.974	76.3	0.999	94.8	0.999	89.3	0.999
	0.7	163.4	0.982	143.4	0.973	140.7	0.974	69.9	0.991	97.9	0.999	92.2	0.998
	0.75	202.7	0.996	163.6	0.980	161.7	0.981	88.8	0.998	129.1	0.989	124.5	0.983
	0.8	241.5	0.985	214.9	0.981	215.3	0.982	110.8	0.941	176.1	0.983	173.7	0.977
Average		188.7 ± 36.6		165.2 ± 30.2		163.5 ± 31.5		86.4 ± 15.6		124.5 ± 32.7		119.6 ± 33.9	

For the oxidative scenario, the three methods initially show a positive slope, and then plunge into a deep valley mid-way into the conversion (Figure 5b). A similar pattern has been reported in the literature [51]. At θ = 0.15–0.2, a gentle slope with a very high correlation of $R^2 > 0.99$ and comparable values of E_θ (148, 158, 157 kJ/mol) was observed for the three methods. These values compare well with the published data for the E_θ of *Lentinula edodes* pileus in a similar decomposition range [50]. Wu et al. [51] suggested the reactions here involve the oxidative breakdown of hemicellulose, pectin, and N-containing compounds. Although the activation energies for FWO and STK are about 160 kJ/mol, DFM displays a sharp rise in slope from 164 to 279 kJ/mol. It is noteworthy that the average value of E_θ in stage II for DFM was much higher than the other stages as well as the other methods. This may be another attestation to the complexity involved in the thermal degradation processes as this stage involves the simultaneous oxidative decomposition of hemicellulose, cellulose, and lignin [51]. Just above θ = 0.5, E_θ decreases to a minimum of around 0.68, then increases. This trend highlights the fact that this is a complex thermal process and the activation energy values obtained are simply "apparent". Therefore, it is not uncommon for the values of E_θ to exhibit a marked variation from the intrinsic kinetic

parameters of an individual step [58]. Unlike the pyrolytic process, the last stage of the oxidative decomposition process involves the combustion of char [51].

Generally, the average values of E_θ for air, for the first and second stages of decomposition, are much higher than for N_2. For instance, the Friedman model at the second stage had E_θ = 202 and 137 kJ/mol for air and N_2, respectively. This observation has been previously observed [1]. The implication of this lower energy barrier is required for the reaction to proceed in an inert environment. Significantly, the average values of E_θ in the final decomposition stage for N_2 were higher than in air. For instance, E_θ for the FWO method in air and N_2 gave 125 and 165 kJ/mol, respectively. This may be due to the distinct phenomenon in an inert environment resulting in char formation, while in air it is combusted [51,53]. These results show that both the pyrolytic and the oxidative processes involve complicated, multi-step reaction mechanisms.

3.3.2. Model-Fitting Technique

Table 7 shows the values of E_θ, R^2, and A at different heating rates derived from the CR model for the GG samples. These were deduced from the slope of linear plots of $\ln\left(\frac{g(\theta)}{T^2}\right)$ against the reciprocal of temperature. The reaction order, n, may be taken as a positive or negative integer. However, it is more practicable to define it as Equation (9) [58].

$$0 \leq n \leq 3 \tag{16}$$

There is a postulation that compares the average value of E_θ obtained from the CR method with that of an iso-conversional technique such as FWO. This provides a means to choose an appropriate decomposition mechanism [8,59]. The closest E_θ among the given integral models is believed to represent a probable reaction mechanism. In this investigation, this postulation was employed. Some non-realistic values were obtained for some models and stages of decomposition; therefore, the values of E_θ that had the same order of magnitude as the model-free kinetic data were the only ones considered. Only the data from stage II decomposition satisfy this criterion and therefore are presented for discussion in Table 7. A strong correlation ($R^2 > 0.9$) was demonstrated for all the heating rates in both conditions—implying that the models fairly approximate the decomposition process. Of all the models, as listed in Table 2, it was demonstrated that only two of them, namely chemical reaction and diffusional, represent the probable mechanism that predominates the thermal process. This validates the assertion from the iso-conversional approximation regarding the multi-step reaction pathways and the associated complexities of GG thermal decomposition. The activation energy and the pre-frequency exponential factor, for the integral model, increase with the heating rates. For the chemical reaction model, they increase with an increase in reaction order.

For β 5, 10, 20, and °C/min under N_2, the values of E_θ for the second-order reaction model were 88.3, 102, and 103 kJ/mol, respectively, while the third-order reactions were, respectively, 109, 126, and 127 kJ/mol. In both (N_2 and air) conditions, the diffusional model presents the highest average value of 216 kJ/mol (air) and 137 kJ/mol (N_2). For the second stage of decomposition, the closest average value of E_θ for the FWO (129 kJ/mol) and CR (130 kJ/mol) models in the N_2 atmosphere represents the diffusional model. This suggests the critical role of diffusion in this stage of decomposition for the tropical grass being investigated. It has been reported in the literature that where the mobility of the reactant constituents depends on the lattice defects, the solid-state reactions mostly occur between either the molecules penetrating the lattices or the crystal lattices [59].

Table 7. Values of E_θ (kJ/mol), R^2, and A (min^{-1}) for N_2 and air atmospheres (stage II) based on Coats–Redfern model.

N_2	5 °C/min			10 °C/min			20 °C/min			Average		
$g(\theta)$	E_θ	R^2	A	E_θ	R^2	A	E_θ	R^2	A	E_θ	R^2	A
Chemical reaction model												
$(1-(1-\theta))^{-1}/(-1)$	88.3	0.966	1.04×10^9	101.9	0.990	2.83×10^{10}	102.8	0.991	3.99×10^{10}	99.8	0.985	2.31×10^{10}
$(1-(1-\theta))^{-2}/(-2)$	108.7	0.954	1.22×10^{11}	126.2	0.983	6.67×10^{12}	127.3	0.983	8.42×10^{12}	123.4	0.976	5.07×10^{12}
Diffusional model												
θ^2	102.6	0.985	5.40×10^9	118.0	0.999	1.97×10^{11}	119.1	0.999	2.58×10^{11}	115.7	0.996	1.53×10^{11}
$(1-\theta)*\ln(1-\theta)+\theta$	111.4	0.982	2.1×10^{10}	128.3	0.999	1.02×10^{12}	129.4	0.999	1.28×10^{12}	125.7	0.994	7.74×10^{11}
$\left(1-(1-\theta)^{1/3}\right)^2$	121.4	0.979	4.78×10^{10}	140.1	0.997	3.24×10^{12}	141.3	0.997	3.83×10^{12}	137.2	0.993	2.37×10^{12}
$1-(2/3)\theta-(1-\theta)^{2/3}$	114.7	0.981	1.01×10^{10}	132.2	0.998	5.50×10^{11}	133.4	0.998	6.74×10^{11}	129.5	0.994	4.11×10^{11}
Air												
Chemical reaction model												
$(1-(1-\theta))^{-1}/(-1)$	105.7	0.997	7.24×10^{10}	124.1	0.989	6.42×10^{12}	121.9	0.976	5.09×10^{12}	156.7	0.985	3.86×10^{12}
$(1-(1-\theta))^{-2}/(-2)$	131.0	0.999	3.05×10^{13}	155.1	0.991	7.23×10^{15}	152.5	0.980	4.65×10^{15}	196.2	0.986	3.97×10^{15}
Diffusional model												
θ^2	120.4	0.984	4.84×10^{11}	142.2	0.974	7.47×10^{13}	139.1	0.953	4.52×10^{13}	180.8	0.973	4.01×10^{13}
$(1-\theta)*\ln(1-\theta)+\theta$	131.3	0.986	3.13×10^{12}	155.2	0.977	7.27×10^{14}	151.9	0.958	3.99×10^{14}	197.4	0.976	3.76×10^{14}
$\left(1-(1-\theta)^{1/3}\right)^2$	143.7	0.990	1.29×10^{13}	170.1	0.980	4.82×10^{15}	166.6	0.962	2.37×10^{15}	216.4	0.978	2.40×10^{15}
$1-(2/3)\theta-(1-\theta)^{2/3}$	135.4	0.988	1.84×10^{12}	160.1	0.978	4.99×10^{14}	156.7	0.959	2.65×10^{14}	203.7	0.977	2.55×10^{14}

3.3.3. Combustion Characteristics

Table 8 presents the combustion characteristics of GG at different heating rates based on the TGA data and Equations (9)–(12). It is shown that the ignition and burnout temperatures rise with the increasing heating rate, while the corresponding time decreases. The combustion performance indices, S, C, D_i, and D_b, all increased with the heating rate. This highlights the fact that the combustion efficiency increases with the heating rate. This same trend has been observed in the published literature [8]. A correlation analysis was conducted using Pearson's coefficient, r, for the combustion atmosphere ($n = 3$). It was shown that the heating rate had a significantly positive correlation with the $-Rp$ ($p \leq 0.03$), Rv ($p \leq 0.0001$), and C ($p \leq 0.03$), whereas it showed no significant positive correlation with T_i, T_b, S, D_i, and D_b ($p > 0.05$). A similar finding, with the exception of comprehensive combustibility, S, was observed in the combustion study of tea leaves and waste teas [57]. The values of the indices obtained were of the same order of magnitude for nearly all the heating rates that were reported by Chen et al. [8] and Cai et al. [57]. In comparison with other lignocellulosic biomass in relation to their ignition temperatures at 10 °C/min (Pinus: 243 °C, 12 min [8]; Jackfruit peel: 213 °C, 18 min; Jackfruit seed: 246 °C, 21 min [39]; Tamarind husk: 240 °C, 21 min; Tamarind seed: 250 °C, 22 min [42]), the ignition temperature and time of the GG were higher. This implies that the ignition process for the GG may be relatively more difficult.

Table 8. Combustion characteristics of GG at different heating rates.

β	Temperature (K)			Time (min)				Combustion Characteristics					
(K/min)	T_i	T_{max}	T_b	t_i	t_p	t_b	$\Delta t_{1/2}$	$-R_p$ (%/min)	$-R_v$ (%/min)	$S \times 10^{-7}$ (%^{2}/(min^2∗K^3))	$C \times 10^{-5}$ (%/(min∗K^2))	$D_i \times 10^{-2}$ (%/min^3)	$D_b \times 10^{-3}$ (%/min^4)
5	528.6	562.8	732.1	47.05	54.05	90.20	60.00	4.15	0.50	0.10	1.49	0.16	0.014
10	544.7	580.4	734.2	25.00	28.60	45.15	26.20	11.15	1.00	0.51	3.76	1.56	0.33
20	555.7	589.4	773.6	13.13	14.80	24.63	22.82	23.11	2.00	1.93	7.49	11.9	2.78

3.3.4. Thermodynamics Analysis

Table 9 shows the thermodynamic parameters for the thermal decomposition of GG at 20 K/min in N_2 and air atmospheres. These values were calculated from the apparent activation energy E_θ based on DFM and a first-order differential model. The choice of DFM was informed by the fact that the temperature function was not modeled as an integral approximation, and the result may thus be expected to be relatively more accurate. Though the global reaction mechanism was assumed here, it is noteworthy that the underlying principle for iso-conversional methods supposes that the description of the process kinetics is based on multiple single-step kinetic equations, in which each equation is associated with a given conversion extent over a narrow temperature range, thus validating the use of the DFM model. The model was used for the computation of the pre-exponential frequency factor (A), which gives insight into the frequency of collisions between reactants [60]. It has been shown that for pre-exponential factor values with orders of magnitude $\leq 10^9$ min^{-1}, the surface reaction pathway is predominantly manifested [61]—this pathway was clearly noticeable for $\theta = 0.6 - 0.7$, in the air atmosphere. The ΔH was negatively correlated with the conversion for air (r = −0.27; $p < 0.05$), while it was positively correlated for N_2 (r = 0.84; $p < 0.05$). The average value of ΔH for decomposition in the air (156 kJ/mol) is higher than for N_2 (142 kJ/mol)—an indication of a relatively higher reactivity in an oxidative reaction, as earlier noted. Zou et al. [50] observed that the ΔH is a reflection of the exchange of heat between complex activated species and reactants so that the higher the value, the higher the reactivity and the faster the rate of reaction. It has been noted that a positive value of ΔH indicates an endothermic reaction [8]. By implication, the pyrolytic and oxidative processes were endothermic throughout the conversion range. The average values of ΔH obtained in this study for both thermal conditions are higher than that for peanut shells, (74.8 kJ/mol; air) and (29.3 kJ/mol; N_2) [1]. The values of ΔG for both atmospheres were positively correlated with conversion. The ΔG is an indication of

the total energy increase for the reaction in a thermal degradation process and portrays the difficulty and direction of the reactions. Chen et al. [8] stated that large values of ΔG are suggestive of the low possibility of reactions, and positive values indicate non-spontaneity in reactions. The mean values of ΔG for thermal degradation in N_2 and air are 143 and 135 kJ/mol, respectively. This conforms with the findings in the literature [1]. This suggests a less favorable reaction of GG in N_2 relative to air. In addition, it may be inferred that both the oxidative and pyrolytic processes of GG proceeded in a non-spontaneous manner. Ahmad et al. [60] opined that ΔG is a measure of the amount of energy that is available from the thermal degradation of a given biomass. In comparison to peanut shells and red pepper waste, the thermal decomposition of GG will generate more energy [1,62], whereas it will liberate relatively less energy than Camel grass and Napier grass [38,63]. Generally, the ΔS provides information on the degree of disorder for the reactions taking place in the thermal decomposition process. Unlike in air ($r = -0.33$; $p < 0.05$), the values of ΔS for N_2 ($r = 0.84$; $p < 0.05$) were positively correlated with conversion. The trend for ΔS was quite similar to that reported by Cai et al. [57] for tea leaves in a N_2/O_2 atmosphere and that by Ahmad et al. [64] for Para grass, particularly with respect to the appearances of positive and negative values, whereas in air, at $\theta \leq 0.55$, which corresponds mainly to hemicellulose and cellulose decomposition, ΔS had positive values and ΔS in N_2, at $\theta \leq 0.40$, had negative values. This may suggest that the earlier stages of the pyrolytic process had a relatively lower degree of disorder for the product formation, while the converse was true for the oxidative process. Significantly, the dominancy of ΔS positive values, which attests to a high degree of disorder for the thermal processes, has been observed in the literature [57]. The average value of ΔS in N_2 (0.043 kJ/(mol*K) is lower than in air (0.1132 kJ/(mol*K).

Table 9. Thermodynamic parameters for GG thermal decomposition at 20 K/min based on DFM.

	N_2				Air			
θ	A (min^{-1})	ΔH (kJ/mol)	ΔG (kJ/mol)	ΔS (kJ/(mol∗K))	A (min^{-1})	ΔH (kJ/mol)	ΔG (kJ/mol)	ΔS (kJ/(mol∗K))
0.15	3.44×10^{10}	100.96	121.35	−0.0569	2.83×10^{14}	139.21	128.38	0.0184
0.20	2.28×10^{10}	101.61	123.56	−0.0613	1.44×10^{15}	147.17	128.47	0.0317
0.25	5.98×10^{11}	117.47	129.85	−0.0346	1.72×10^{16}	159.03	128.27	0.0522
0.30	1.83×10^{12}	123.21	132.35	−0.0255	7.04×10^{17}	176.86	127.96	0.0830
0.35	3.14×10^{12}	126.47	133.92	−0.0212	8.41×10^{18}	189.12	128.10	0.1035
0.40	3.82×10^{12}	127.90	134.83	−0.0198	1.47×10^{21}	214.60	128.31	0.1464
0.45	6.10×10^{13}	142.37	141.25	0.0031	5.57×10^{23}	244.24	128.90	0.1957
0.50	1.36×10^{14}	146.94	143.48	0.0097	1.80×10^{26}	274.13	130.50	0.2437
0.55	8.32×10^{12}	132.88	137.79	−0.0137	1.13×10^{21}	219.84	134.97	0.1440
0.60	1.03×10^{13}	134.64	138.97	−0.0121	4.21×10^{9}	95.115	139.29	−0.0750
0.65	3.29×10^{13}	141.88	142.79	−0.0025	1.82×10^{7}	71.052	142.09	−0.1205
0.7	4.54×10^{14}	158.00	151.15	0.0191	2.85×10^{6}	64.410	144.75	−0.1363
0.75	2.54×10^{17}	197.27	171.65	0.0715	5.87×10^{7}	83.028	148.80	−0.1116
0.8	3.82×10^{17}	235.88	195.51	0.1126	7.78×10^{25}	104.80	152.79	−0.0814
Average	4.55×10^{16}	141.97	142.75	0.0432	1.85×10^{25}	155.90	135.11	0.1132

4. Conclusions

Guinea grass (*Megathyrsus maximus*) was subjected to thermal degradation in a non-isothermal TGA (N_2 inert and dry air atmosphere) at multiple heating rates of 5, 10, and 20 K/min. The Coats–Redfern, Flynn–Wall–Ozawa, and Starink techniques were utilized to evaluate the kinetic parameters, and these were subsequently used in the combustion characteristics and thermodynamics analyses. A couple of integral models, representative of various decomposition mechanisms, was tested in the model-fitting technique. This was with the primary objective of evaluating the bioenergy potential of GG.

The thermal profile of the GG proceeded distinctly under the different heating scenarios—the average residual mass after the GG decomposition was 29.1% and 13.2%, respectively, for the N_2 and air environments. The model-fitting technique suggested that the chemical reaction and diffusional models play critical roles in the thermal decomposition processes of GG, both in the N_2 and the air atmospheres. The kinetics model also revealed three distinctive stages of decomposition, which correspond to moisture

evaporation, devolatilization, and solid residue burnout/char formation. On average, the activation energy for the decomposition in the air is relatively higher than in the N_2 atmosphere. The decomposition process in air showed relatively higher reactivity, with an average value enthalpy change being 156 kJ/mol, as opposed to 141 kJ/mol for the N_2 environment. According to the change in Gibbs free energy, it was also shown that both processes proceeded in a non-spontaneous manner. It may be concluded from the foregoing that the thermal decomposition process of GG, either in an N_2-pyrolytic or oxidative environment, follows a complex pathway that involves parallel and successive reactions. It has been demonstrated that GG would be a suitable feedstock for biofuel production and bioenergy purposes. The information derived from the combustion characteristics would be useful in the development and application of combustion technology for the GG.

Author Contributions: A.O.B., A.A.A. and P.P.I. conceived the research idea; A.O.B., A.A.A., P.P.I. and S.O.A. provided the materials for the research; A.O.B., A.A.A. and P.P.I. did the preliminary sample preparation in the laboratory; A.M.A. and A.G.M. carried out the further laboratory experiments on the prepared samples to obtain the required data; A.O.B. did the data analyses and wrote the first draft of the manuscript; A.A.A., P.P.I., S.O.A., A.M.A. and A.G.M. contributed to the scientific discussion of the manuscript. All authors have read and agreed to the published version of the manuscript.

Funding: This research received no external funding.

Data Availability Statement: The data presented in this study are available on request from the corresponding author.

Conflicts of Interest: The authors declare no conflict of interest.

References

1. Xu, Z.; Xiao, X.; Fang, P.; Ye, L.; Huang, J.; Wu, H.; Tang, Z.; Chen, D. Comparison of combustion and pyrolysis behavior of the peanut shells in air and N_2: Kinetics, thermodynamics and gas emissions. *Sustainability* **2020**, *12*, 464. [CrossRef]
2. Li, Q.; Zhao, C.; Chen, X.; Wu, W.; Li, Y. Comparison of pulverized coal combustion in air and in O_2/CO_2 mixtures by thermo-gravimetric analysis. *J. Anal. Appl. Pyrolysis* **2009**, *85*, 521–528. [CrossRef]
3. Sattar, H.; Muzaffar, I.; Munir, S. Thermal and kinetic study of rice husk, corn cobs, peanut crust and Khushab coal under inert (N_2) and oxidative (dry air) atmospheres. *Renew. Energy* **2020**, *149*, 794–805. [CrossRef]
4. Rueda-Ordóñez, Y.J.; Tannous, K. Thermal decomposition of sugarcane straw, kinetics and heat of reaction in synthetic air. *Bioresour. Technol.* **2016**, *211*, 231–239. [CrossRef] [PubMed]
5. Lasode, O.A.; Balogun, A.O.; McDonald, A.G. Torrefaction of some Nigerian lignocellulosic resources and decomposition kinetics. *J. Anal. Appl. Pyrolysis* **2014**, *109*, 47–55. [CrossRef]
6. Lisseth, C.; Martinez, M.; Patrícia, E.; Rocha, A.; Cassia, A.d.C.O.; Carneiro, O.; José, F.; Gomes, B.; Aparecida, L.; Batalha, R.; et al. Characterization of residual biomasses from the coffee production chain and assessment the potential for energy purposes. *Biomass Bioenergy* **2019**, *120*, 68–76.
7. Balogun, A.O.; Lasode, O.A.; McDonald, A.G. Devolatilisation kinetics and pyrolytic analyses of Tectona grandis (teak). *Bioresour. Technol.* **2014**, *156*, 57–62. [CrossRef] [PubMed]
8. Chen, R.; Li, Q.; Xu, X.; Zhang, D.; Hao, R. Combustion characteristics, kinetics and thermodynamics of Pinus Sylvestris pine needle via non-isothermal thermogravimetry coupled with model-free and model-fitting methods. *Case Stud. Therm. Eng.* **2020**, *22*, 100756. [CrossRef]
9. Azeez, A.M.; Meier, D.; Odermatt, J. Temperature dependence of fast pyrolysis volatile products from European and African biomasses. *J. Anal. Appl. Pyrolysis* **2011**, *90*, 81–92. [CrossRef]
10. Adesemuyi, M.F.; Adebayo, M.A.; Akinola, A.O.; Olasehinde, E.F.; Adewole, K.A.; Lajide, L. Preparation and characterisation of biochars from elephant grass and their utilisation for aqueous nitrate removal: Effect of pyrolysis temperature. *J. Environ. Chem. Eng.* **2020**, *8*, 1–12. [CrossRef]
11. Mohammed, I.Y.; Abakr, Y.A.; Mokaya, R. Biofuel and valuable products recovery from Napier grass pre-processing: Process design and economic analysis. *J. Environ. Chem. Eng.* **2019**, *7*, 102962. [CrossRef]
12. Awasthi, A.; Singh, G.; Dhyani, V.; Kumar, J.; Reddy, Y.S.; Adarsh, V.P.; Puthiyamadam, A.; Mullepureddy, K.K.; Sukumaran, R.K.; Ummalyma, S.B.; et al. Co-pyrolysis of phumdi and para grass biomass from Loktak Lake. *Bioresour. Technol.* **2019**, *285*, 1–6. [CrossRef]
13. Cai, X.; Zhang, X.; Wang, D. Land availability for biofuel production. *Environ. Sci. Technol.* **2011**, *45*, 334–339. [CrossRef] [PubMed]
14. Kumar, S.; Ghosh, P. Sustainable bio-energy potential of perennial energy grass from reclaimed coalmine spoil (marginal sites) of India. *Renew. Energy* **2018**, *123*, 475–485. [CrossRef]

15. Mohapatra, S.; Mishra, C.; Behera, S.S.; Thatoi, H. Application of pretreatment, fermentation and molecular techniques for enhancing bioethanol production from grass biomass—A review. *Renew. Sustain. Energy Rev.* **2017**, *78*, 1007–1032. [CrossRef]
16. Tan, K.T.; Lee, K.T.; Mohamed, A.R. Role of energy policy in renewable energy accomplishment: The case of second-generation bioethanol. *Energy Policy* **2008**, *36*, 3360–3365. [CrossRef]
17. Egwu, U.; Sallis, P.; Oko, E. Study of the impacts of supplements on the specific methane production during anaerobic digestion of the West African Gamba and Guinea Grass. *Fuel* **2021**, *285*, 1–10. [CrossRef]
18. Brosse, N.; Dufour, A.; Meng, X.; Sun, Q.; Ragauskas, A. Miscanthus: A fast-grwoing crop for biofuels and chemicals production. *Biofuels Bioprod. Biorefining* **2012**, *6*, 580–598. [CrossRef]
19. Balogun, A.O.; Lasode, O.A.; McDonald, A.G. Thermo-analytical and physico-chemical characterization of woody and non-woody biomass from an agro-ecological zone in Nigeria. *BioResources* **2014**, *9*, 5099–5113. [CrossRef]
20. Ajimotokan, H.A.; Ehindero, A.O.; Ajao, K.S.; Adeleke, A.A.; Ikubanni, P.P.; Shuaib-Babata, Y.L. Combustion characteristics of fuel briquettes made from charcoal particles and sawdust agglomerates. *Sci. Afr.* **2019**, *6*, 1–9. [CrossRef]
21. Xu, F.; Yu, J.; Tesso, T.; Dowell, F.; Wang, D. Qualitative and quantitative analysis of lignocellulosic biomass using infrared techniques: A mini-review. *Appl. Energy* **2013**, *104*, 801–809. [CrossRef]
22. Balogun, A.O.; Sotoudehniakarani, F.; Mcdonald, A.G. Thermo-kinetic, spectroscopic study of brewer's spent grains and characterisation of their pyrolysis products. *J. Anal. Appl. Pyrolysis* **2017**, *127*, 8–16. [CrossRef]
23. Singh, Y.D.; Mahanta, P.; Bora, U. Comprehensive characterization of lignocellulosic biomass through proximate, ultimate and compositional analysis for bioenergy production. *Renew. Energy* **2017**, *103*, 490–500. [CrossRef]
24. Hameed, S.; Sharma, A.; Pareek, V.; Wu, H.; Yu, Y. A review on biomass pyrolysis models: Kinetic, network and mechanistic models. *Biomass Bioenergy* **2019**, *123*, 104–122. [CrossRef]
25. Papari, S.; Hawboldt, K. A review on the pyrolysis of woody biomass to bio-oil: Focus on kinetic models. *Renew. Sustain. Energy Rev.* **2015**, *52*, 1580–1595. [CrossRef]
26. Masnadi, M.S.; Habibi, R.; Kopyscinski, J.; Hill, J.M.; Bi, X.; Lim, C.J.; Ellis, N.; Grace, J.R. Fuel characterization and co-pyrolysis kinetics of biomass and fossil fuels. *Fuel* **2014**, *117*, 1204–1214. [CrossRef]
27. Almazrouei, M.; Janajreh, I. Model-fitting approach to kinetic analysis of non-isothermal pyrolysis of pure and crude glycerol. *Renew. Energy* **2020**, *145*, 1693–1708. [CrossRef]
28. Ashraf, A.; Sattar, H.; Munir, S.; Husk, R. A comparative applicability study of model-fitting and model-free kinetic analysis approaches to non-isothermal pyrolysis of coal and agricultural residues. *Fuel* **2019**, *240*, 326–333. [CrossRef]
29. Haykırı-açma, H.; Yaman, S. Kinetic modelling of RDF pyrolysis: Model-fitting and model-free approaches. *Waste Manag.* **2016**, *48*, 275–284.
30. Ali, I.; Raza, S.; Bahadar, A. Kinetic analysis of Botryococcus braunii pyrolysis using model-free and model fitting methods. *Fuel* **2018**, *214*, 369–380. [CrossRef]
31. Amoo, L.M. Computational fluid dynamics simulation of Lafia-Obi bituminous coal in a fluidized-bed chamber for air- and oxy-fuel combustion technologies. *Fuel* **2015**, *140*, 178–191. [CrossRef]
32. Wilk, M.; Magdziarz, A.; Gajek, M.; Zajemska, M.; Jayaraman, K. Combustion and kinetic parameters estimation of torrefied pine, acacia and Miscanthus giganteus using experimental and modelling techniques. *Bioresour. Technol.* **2017**, *243*, 304–314. [CrossRef]
33. Bach, Q.V.; Tran, K.Q.; Skreiberg, Ø. Combustion kinetics of wet-torrefied forest residues using the distributed activation energy model (DAEM). *Appl. Energy* **2017**, *185*, 1059–1066. [CrossRef]
34. Sun, L.; Varanasi, P.; Yang, F.; Loqué, D.; Simmons, B.A.; Singh, S. Rapid determination of syringyl: Guaiacyl ratios using FT-Raman spectroscopy. *Biotechnol. Bioeng.* **2012**, *109*, 647–656. [CrossRef] [PubMed]
35. Balogun, A.O.; McDonald, A.G. Decomposition kinetic study, spectroscopic and pyrolytic analyses of Isoberlinia doka and Pinus ponderosa. *Biomass Convers. Biorefinery* **2016**, *6*, 315–324. [CrossRef]
36. Cai, J.; Xu, D.; Dong, Z.; Yu, X.; Yang, Y.; Banks, S.W.; Bridgwater, A.V. Processing thermogravimetric analysis data for isoconversional kinetic analysis of lignocellulosic biomass pyrolysis: Case study of corn stalk. *Renew. Sustain. Energy Rev.* **2018**, *82*, 2705–2715. [CrossRef]
37. Martínez-Ramírez, S.; Frías, M.; Nakanishi, E.Y.; Savastano, H. Pozzolanic Reaction of a Biomass Waste as Mineral Addition to Cement Based Materials: Studies by Nuclear Magnetic Resonance (NMR). *Int. J. Concr. Struct. Mater.* **2019**, *13*, 1–8. [CrossRef]
38. Mehmood, M.A.; Ye, G.; Luo, H.; Liu, C.; Malik, S.; Afzal, I.; Xu, J.; Ahmad, M.S. Pyrolysis and kinetic analyses of Camel grass (Cymbopogon schoenanthus) for bioenergy. *Bioresour. Technol.* **2017**, *228*, 18–24. [CrossRef] [PubMed]
39. Alves, J.L.F.; da Silva, J.C.G.; Mumbach, G.D.; di Domenico, M.; da Silva Filho, V.F.; de Sena, R.F.; Machado, R.A.F.; Marangoni, C. Insights into the bioenergy potential of jackfruit wastes considering their physicochemical properties, bioenergy indicators, combustion behaviors, and emission characteristics. *Renew. Energy* **2020**, *155*, 1328–1338. [CrossRef]
40. Aganga, A.A.; Tshwenyane, S. Potentials of Guinea Grass (Panicum maximum) as Forage Crop in Livestock Production. *Pakistan J. Nutr.* **2004**, *3*, 1–4.
41. Mohammed, I.Y.; Abakr, Y.A.; Kazi, F.K.; Yusup, S.; Alshareef, I.; Chin, S.A. Comprehensive Characterization of Napier Grass as a Feedstock for Thermochemical Conversion. *Energies* **2015**, *8*, 3403–3417. [CrossRef]
42. Alves, J.L.F.; da Silva, J.C.G.; Mumbach, G.D.; di Domenico, M.; de Sena, R.F.; Machado, R.A.F.; Marangoni, C. Demonstrating the Suitability of Tamarind Residues to Bioenergy Exploitation Via Combustion Through Physicochemical Properties, Performance Indexes, and Emission Characteristics. *Bioenergy Res.* **2020**, *13*, 1308–1320. [CrossRef]

43. Alves, J.L.F.; da Silva, J.C.G.; Mumbach, G.D.; da Silva Filho, V.F.; Di Domenico, M.; de Sena, R.F.; Bolzan, A.; Machado, R.A.F.; Marangoni, C. Thermo-kinetic investigation of the multi-step pyrolysis of smoked cigarette butts towards its energy recovery potential. *Biomass Convers. Biorefinery* **2020**, 1–15. [CrossRef]
44. Gandra, J.R.; de Oliveira, E.R.; de Goes, R.H.T.B.; de Oliveira, K.M.P.; Takiya, C.S.; Del Valle, T.A.; Araki, H.M.C.; Silveira, K.; SIlva, D.; da Silva Pause, A.G. Microbial inoculant and an extract of Trichoderma longibrachiatum with xylanase activity effect on chemical composition, fermentative profile and aerobic stability of guinea grass (Pancium maximum Jacq.) silage. *J. Anim. Feed Sci.* **2017**, *26*, 339–347. [CrossRef]
45. Ratsamee, S.; Akaracharanya, A.; Leepipatpiboon, N.; Srinorakutara, T.; Kitpreechavanich, V.; Tolieng, V. Purple guinea grass: Pretreatment and ethanol fermentation. *BioResources* **2012**, *7*, 1891–1906. [CrossRef]
46. Detmann, E.; de Oliveira Franco, M.; Íris Gomes, D.; Medrado Barbosa, M.; de Campos Valadares Filho, S. Protein contamination on Klason lignin contents in tropical grasses and legumes. *Pesq. Agropec. Bras* **2014**, *49*, 994–997. [CrossRef]
47. Clapham, W.M.; Foster, J.G.; Neel, J.P.S. Fatty Acid Composition of Traditional and Novel Forages. *J. Agric. Food Chem.* **2005**, *53*, 10068–10073. [CrossRef] [PubMed]
48. Luengnaruemitchai, A.; Anupapwisetkul, C. Surface morphology and cellulose structure of Napier grass pretreated with the ionic liquid 1-ethyl-3-methylimidazolium acetate combined with either water or dimethyl sulfoxide as a co-solvent under microwave irradiation. *Biomass Convers. Biorefinery* **2020**, *10*, 435–446. [CrossRef]
49. Li, H.; McDonald, A.G. Fractionation and characterization of industrial lignins. *Ind. Crops Prod.* **2014**, *62*, 67–76. [CrossRef]
50. Zou, H.; Evrendilek, F.; Liu, J.; Buyukada, M. Combustion behaviors of pileus and stipe parts of Lentinus edodes using thermogravimetric-mass spectrometry and Fourier transform infrared spectroscopy analyses: Thermal conversion, kinetic, thermodynamic, gas emission and optimization analyses. *Bioresour. Technol.* **2019**, *288*, 121481. [CrossRef] [PubMed]
51. Wu, W.; Mei, Y.; Zhang, L.; Liu, R.; Cai, J. Kinetics and reaction chemistry of pyrolysis and combustion of tobacco waste. *Fuel* **2015**, *156*, 71–80. [CrossRef]
52. Ding, Y.; Huang, B.; Wu, C.; He, Q.; Lu, K. Kinetic model and parameters study of lignocellulosic biomass oxidative pyrolysis. *Energy* **2019**, *181*, 11–17. [CrossRef]
53. Greenhalf, C.E.; Nowakowski, D.J.; Bridgwater, A.V.; Titiloye, J.; Yates, N.; Riche, A.; Shield, I. Thermochemical characterisation of straws and high yielding perennial grasses. *Ind. Crops Prod.* **2012**, *36*, 449–459. [CrossRef]
54. Alvarenga, L.M.; Xavier, T.P.; Barrozo, M.A.S.; Bacelos, M.S.; Lira, T.S. Analysis of reaction kinetics of carton packaging pyrolysis. *Procedia Eng.* **2012**, *42*, 113–122. [CrossRef]
55. Gogoi, M.; Konwar, K.; Bhuyan, N.; Chandra, R. Assessments of pyrolysis kinetics and mechanisms of biomass residues using thermogravimetry. *Bioresour. Technol. Rep.* **2018**, *4*, 40–49. [CrossRef]
56. Wang, X.; Hu, M.; Hu, W.; Chen, Z.; Liu, S.; Hu, Z.; Xiao, B. Thermogravimetric kinetic study of agricultural residue biomass pyrolysis based on combined kinetics. *Bioresour. Technol.* **2016**, *219*, 510–520. [CrossRef] [PubMed]
57. Cai, H.; Zou, H.; Liu, J.; Xie, W.; Kuo, J.; Buyukada, M.; Evrendilek, F. Thermal degradations and processes of waste tea and tea leaves via TG-FTIR: Combustion performances, kinetics, thermodynamics, products and optimization. *Bioresour. Technol.* **2018**, *268*, 715–725. [CrossRef]
58. Vyazovkin, S.; Burnham, A.K.; Criado, J.M.; Pérez-Maqueda, L.A.; Popescu, C.; Sbirrazzuoli, N. ICTAC Kinetics Committee recommendations for performing kinetic computations on thermal analysis data. *Thermochim. Acta* **2011**, *520*, 1–19. [CrossRef]
59. Ding, Y.; Ezekoye, O.A.; Lu, S.; Wang, C.; Zhou, R. Comparative pyrolysis behaviors and reaction mechanisms of hardwood and softwood. *Energy Convers. Manag.* **2017**, *132*, 102–109. [CrossRef]
60. Ahmad, M.S.; Mehmood, M.A.; Taqvi, S.T.H.; Elkamel, A.; Liu, C.G.; Xu, J.; Rahimuddin, S.A.; Gull, M. Pyrolysis, kinetics analysis, thermodynamics parameters and reaction mechanism of Typha latifolia to evaluate its bioenergy potential. *Bioresour. Technol.* **2017**, *245*, 491–501. [CrossRef]
61. Badshah, S.L.; Shah, Z.; Alves, J.L.F.; da Silva, J.C.G.; Noreen, N.; Iqbal, A. Kinetic and thermodynamics study of the pyrolytic process of the freshwater macroalga, Chara vulgaris. *J. Appl. Phycol.* **2021**, *33*, 2511–2521. [CrossRef]
62. Maia, A.A.D.; de Morais, L.C. Kinetic parameters of red pepper waste as biomass to solid biofuel. *Bioresour. Technol.* **2016**, *204*, 157–163. [CrossRef] [PubMed]
63. Manatura, K. Napier Grass Pyrolysis: Kinetic and Thermodynamics Analysis. *RMUTI J. Sci. Technol.* **2019**, *12*, 1–13.
64. Ahmad, M.S.; Mehmood, M.A.; Al Ayed, O.S.; Ye, G.; Luo, H.; Ibrahim, M.; Rashid, U.; Arbi Nehdi, I.; Qadir, G. Kinetic analyses and pyrolytic behavior of Para grass (Urochloa mutica) for its bioenergy potential. *Bioresour. Technol.* **2017**, *224*, 708–713. [CrossRef] [PubMed]